SCIENTIFIC REP⚙RTS

OPEN

Upward shift of the vortex solid phase in high-temperature-superconducting wires through high density nanoparticle addition

Masashi Miura[1,2], Boris Maiorov[1], Fedor F. Balakirev[1], Takeharu Kato[3], Michio Sato[2], Yuji Takagi[4], Teruo Izumi[4] & Leonardo Civale[1]

We show a simple and effective way to improve the vortex irreversibility line up to very high magnetic fields (60T) by increasing the density of second phase $BaZrO_3$ nanoparticles. $(Y_{0.77},Gd_{0.23})Ba_2Cu_3O_y$ films were grown on metal substrates with different concentration of $BaZrO_3$ nanoparticles by the metal organic deposition method. We find that upon increase of the $BaZrO_3$ concentration, the nanoparticle size remains constant but the twin-boundary density increases. Up to the highest nanoparticle concentration ($n \sim 1.3 \times 10^{22}$/m³), the irreversibility field (H_{irr}) continues to increase with no sign of saturation up to 60T, although the vortices vastly outnumber pinning centers. We find extremely high H_{irr}, namely $H_{irr} = 30$T (H||45°) and 24T (H||c) at 65 K and 58T (H||45°) and 45T (H||c) at 50K. The difference in pinning landscape shifts the vortex solid-liquid transition upwards, increasing the vortex region useful for power applications, while keeping the upper critical field, critical temperature and electronic mass anisotropy unchanged.

Although the critical temperature (T_c) and upper critical field (H_{c2}) of high temperature superconductors are extremely high, superconductors only become technically useful at a much lower field-temperature boundary, called the melting, or irreversibility, line. This is due to the appearance of the vortex liquid phase, one of the unique characteristics of these superconductors. In this liquid phase, superconductors have finite resistivity behaving much like a normal metal, thus the need to move the melting line to higher fields/temperatures. Defects can move the melting line, with random point-like defects[1] pushing it down and correlated defects moving this line up. The positive effect of correlated disorder is restricted to an angular range near the defects' orientation, and usually only up to a characteristic field related to the density of the defects (the matching field, typically a few tesla)[2–5]. Pushing up this upper limit is both technologically and scientifically important; given the interest in high magnetic field magnets. This requires finding ways to immobilize vortex densities much higher than the highest defect density that can be introduced without compromising the material integrity.

Recently, a third kind of disorder (neither correlated nor point-like) has been demonstrated to be effective at improving both J_c and H_{irr} at a very wide range of field orientations[6–14]. A deeper and more quantitative understanding of the effect of nanoparticles in a mixed pinning landscape (as they often work together with correlated defects) is necessary for assessing the potential of Cu-based superconducting wires for applications at high fields[15].

In particular, it is important to establish the behavior of H_{irr} when the vortex density is much higher than that of the defects. Most $REBa_2Cu_3O_y$ (REBCO) films (RE = rare earth) with self-assembled nanorods[4,5] and YBCO crystals with columnar defects[2,3] show improved H_{irr} and a "kink" in the vortex liquid-glass transition for **H**||c. This occurs when vortices stop populating columnar defects and start filling interstitial positions, at a density related to that of the defects at the so-called matching field (μ_0H_ϕ). These findings lead to the validation of the

[1]Materials Physics and Applications Division, Los Alamos National Laboratory, Los Alamos, New Mexico 87545, USA. [2]Graduate School of Science & Technology, Seikei University, 3-3-1 Kichijoji-kitamachi, Musashino-shi, Tokyo 180-8633, Japan. [3]Materials R&D Laboratory, Japan Fine Ceramics Center, 2-4-1 Mutsuno, Atuta-ku, Nagoya 456-8587, Japan. [4]Superconductivity Research Laboratory, International Superconductivity Technology Center, KSP R&D Wing A-9F, 3-2-1 Sakado, Takatsu-ku, Kaswasaki-shi, Kanagawa, 213-0012 Japan. Correspondence and requests for materials should be addressed to M.M. (email: masashi-m@st.seikei.ac.jp)

simple argument that once the pinning centers have been outnumbered by vortices, their effect on increasing H_{irr} decreases or may even be washed out. However, this idea overlooks the fact that vortices are interacting elastic objects, which form a lattice with different degrees of order depending on the underlying pinning landscape. The understanding of the physical system adds a layer of complexity when pinning centers of different dimensions (point defects, lines, planes or nanoparticles) are taken into account.

In this paper, we show that the combination of planar twin boundaries (TBs) and a higher density of three dimensional (3D) nanoparticles (NPs) increases H_{irr} at up to 60 T. In the case of TBs there is a clear signature of the matching field at very low fields (0.5 T) but nevertheless, their presence continues to increase H_{irr} up to 60 T. The effect of the NPs is also seen up to 60 T with the additional benefit of their being effective in the entire angular range. We find no signs of saturation in the improvement of H_{irr} up to 3 wt% BaZrO$_3$ (BZO) added to REBCO wire up to the highest field measured (60 T), and obtain record high values.

Results

The results shown are distributed as follows. We start by explaining the growth methods and show superconducting and microstructural studies. We find that the use of (Y,Gd)BCO is beneficial (as compared to YBCO) and that the addition of BZO NPs does not degrade the general properties, and increases twin boundary density. Then we focus on transport measurements in DC and pulsed fields as a function of temperature and field orientation. For the upper critical field, (H_{c2}), the addition of NPs produces no significant changes. For H_{irr}, the scenario is complex and depends on the field magnitude and orientation. For **H**||c, at low fields, twin boundaries dominate the irreversibility line with a matching field observed and a peak as function of field orientation. As the field increases the effects of TBs are less prominent as nanoparticles compete in the vortex localization. At high fields, NPs and TBs cooperate to enhance the H_{irr}. At intermediate angles (e.g. **H**||45°) nanoparticles produce the greatest increase in H_{irr}, showing no saturation up to the highest fields measured. Furthermore, at high fields we obtain a constant improvement of 25% with respect to YBCO films. For **H**|| ab, the changes due to NPs addition are small as compared to other orientations.

Uniformly dispersed BaZrO$_3$ nanoparticles in (Y$_{0.77}$Gd$_{0.23}$)Ba$_2$Cu$_3$O$_y$ wires.

The samples used in this study were 0.5 μ thick films of standard YBCO, (Y$_{0.77}$Gd$_{0.23}$)Ba$_2$Cu$_3$O$_y$ ((Y,Gd)BCO) and BZO-doped (Y,Gd) BCO ((Y,Gd)BCO+BZO) derived from the metal organic deposition (MOD) process, grown on metal substrates. The content of BZO in the films was 1–3 wt%. The film microstructure was studied by several techniques (see Methods). The planar view transmission electron microscopy (TEM) images of standard YBCO, (Y,Gd)BCO with 1wt% BZO (+1BZO) and 3wt% BZO (+3BZO) wires are shown in Fig. 1a–c, respectively. For clarity, the corresponding bottom panels in those figures show schematics of the main defects. All films have a low density ($\sim 0.1 \times 10^{21}$/m^3) of large RE$_2$Cu$_2$O$_5$ (225) precipitates (shown as open circles in the bottom panels) formed during REBCO crystallization from the precursors containing BaF$_2$, RE$_2$Cu$_2$O$_5$ and CuO. In both +1BZO and +3BZO wires, BZO NPs (modal size $\sim$23 nm) are randomly distributed and uniformly dispersed. The average density of these nanoparticles was determined to be $n = 2.9 \times 10^{21}$/m^3 for +1BZO, $n = 7.1 \times 10^{21}$/m^3 for +2BZO (not shown), and $n = 13 \times 10^{21}$/m^3 for +3BZO wires, respectively. Note that the greater than linear dependence of n on BZO% derives from the slight decrease in size of the NPs with increasing BZO density. In addition to the uniformly randomly distributed 3D defects (BZO NPs), all samples, including the standard YBCO, contain high densities of two types of planar (2D) defects, namely c-axis correlated TBs (Fig. 1a–d) and stacking faults (SFs) parallel to the ab plane (Fig. 1e). In some previous studies of MOD REBCO with nanoparticles, it was observed that the SFs cut into the TBs, resulting in discontinuous short length TBs[14]. In contrast, although our +3BZO wire has a high density of SFs as shown in Fig. 1e, the TBs remain connected from the bottom to the surface (Fig. 1d), indicating that the TBs in the BZO NP-doped wire are c-axis correlated pinning centers.

Table 1 shows a summary of the crystallographic and superconducting properties for the YBCO, (Y,Gd)BCO, +1BZO, +2BZO and +3BZO films. No decrease in T_c, or increase of $\delta\omega$ or $\delta\phi$ is observed for the films with BZO inclusions. The only difference found is positive, being that films with Y,Gd have higher T_c and *self-field* $J_c(J_c^{s.f.})$ than the YBCO film, consistent with good crystallinity (unchanged $\delta\omega$, $\delta\phi$). The $J_c^{s.f.}$ values of the +3BZO film at 65 and 77 K are 12.5 and 4.0 MA cm^{-2}, respectively. These $J_c^{s.f.}$ values are almost as high as those of nanocomposite MOD-YBCO thin films on a single crystal substrate[6]. The fact that we maintained (or even improved) $J_c^{s.f.}$ and T_c after adding defects is significant given that in some cases, for films grown by pulsed laser deposition (PLD), T_c and $J_c^{s.f}$ decreased with increasing BZO content due to poor crystallinity, local strain and oxygen deficiency near second phases[16]. The difference in T_c and $J_c^{s.f}$ behavior with BZO% between MOD and PLD processes comes from differences in the formation mechanisms of the BZO/REBCO matrix[17].

Irreversibility line at low and intermediate DC magnetic fields.

To investigate the influence of the density of BZO NPs on the superconducting properties of the glassy phase, we measured the irreversibility temperature T_{irr} (H,θ). Figure 2a–c show T_{irr} (θ) at 0.5, 4 and 15 T for standard YBCO, (Y,Gd)BCO and (Y,Gd) BCO+BZO wires, where θ is the angle between the magnetic field and the c axis.

For the YBCO and (Y,Gd)BCO wires, at low magnetic fields we observe two maxima in T_{irr}, centered at **H**||c ($\theta = 0°$) and **H**||ab ($\theta = 90°$). The peak at **H**||c comes from c-axis correlated defects. The maximum at **H**||ab originates from the electronic-mass anisotropy and the SFs. At intermediate fields (see Fig. 2b), the c-axis peak of T_{irr} in both YBCO and (Y,Gd)BCO becomes very weak, but is evident again at higher fields (see Fig. 2c). We note that the $T_{irr}(\theta)/T_c$ for the YBCO and (Y,Gd)BCO wires are almost identical as shown in inset of Fig. 2, which validates the use of YBCO for the comparison that we are making.

All wires with BZO NPs show an enhanced $T_{irr}(\theta)$ as compared to that of the YBCO and (Y,Gd)BCO wires, and the magnitude of the $T_{irr}(\theta)$ enhancement increases with increasing BZO NP content at all magnetic fields (0.5, 4 and 15 T) and at all angles. The T_{irr} anisotropy, $T_{irr}(||ab)/T_{irr}(||c)$, is also smaller for the +BZO samples and
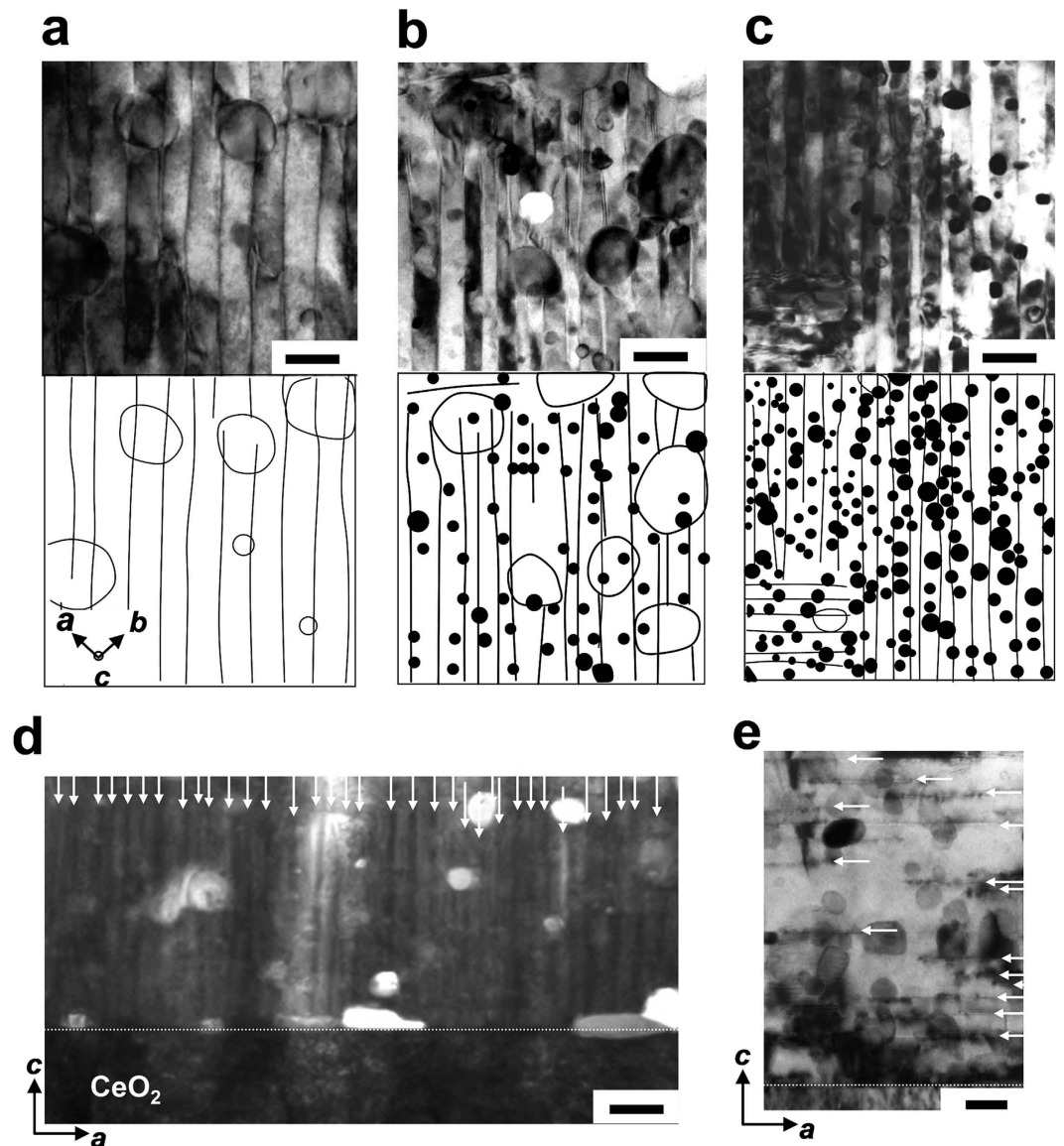
Figure 1. Microstructural characterization for YBCO and (Y,Gd)BCO+BZO wires. Top panels of (**a–c**): High magnification planar view TEM images of (**a**) YBCO, (**b**) +1BZO and (**c**) +3BZO wires, respectively. Bottom row: corresponding positions of TBs and BZO NPs. In the bottom panels, some of the $RE_2Cu_2O_5$ precipitates are indicated by open circles. (**d**) Wide areas of cross-section TEM image of +3BZO wires. The TBs are indicated by arrows. (**e**) Cross-section high-magnification TEM image of +3BZO wire showing randomly dispersed BZO NPs and a high density of SFs (white arrows). Horizontal bars in Fig. 1 (a,b,c,d) and Fig. 1 (e) represent 100 nm and 30 nm, respectively.

decreases monotonically with BZO NP content. At low fields, the +3BZO wire exhibits nearly isotropic properties with a small (in height) c-axis peak. At 15 T, $T_{irr}(\theta)$ shows a small c-axis peak indicating a contribution from correlated pinning. This is consistent with $J_c(\theta)$ data[10] at high fields where a c-axis peak is also found. In both cases (J_c and T_{irr}) the c-axis peak height is less pronounced in samples with BZO additions, partially because of the general increase in J_c and T_{irr} produced by the nanoparticles.

The results in Fig. 2 can be interpreted as follows. At low fields, below the matching field of the TBs ($\mu_0H_{\phi,TB}$) given by $\mu_0H_{\phi,TB} = (\phi_0/d_{TB}^2)$, where ϕ_0 and d_{TB} are the flux quantum and TB spacing respectively, most vortices get localized by the TBs (Fig. 3a). At intermediate H, above $\mu_0H_{\phi,TB}$, the density of vortices is high enough that the TBs become "saturated", the extra vortices sit outside them and become localized by the randomly distributed NPs which are strong pinning centers (Figs 2b and 3b). At even higher fields, once all the NPs are saturated, no elastic energy is lost by achieving pinning at the TBs, allowing for the localization effect of the TBs to be observed through the caging effect (Fig. 3c), similar to what happens for the standard YBCO sample (Fig. 2c).

To better determine the effects of the c-axis correlated defects, we measured $\mu_0H_{irr}(T)$ at low fields for different θ (see Fig. 4). The c-axis irreversibility lines of the wires with and without BZO NPs exhibit a pronounced kink indicating a crossover field (see H_{cr} arrows). For fields smaller than μ_0H_{cr}, H_{irr} shows a rapid increase with

Sample	YBCO	(Y,Gd)BCO	+1BZO	+2BZO	+3BZO
$\delta\omega$ (deg.)	1.07	1.10	1.05	1.08	1.11
$\delta\phi$ (deg.)	2.89	2.85	2.88	2.84	2.83
Average NP diameter (nm)	~108*	~113*	23 ± 4.8	23 ± 4.6	22 ± 4.7
Average NP density (10^{21}/m³)	~0.1*	~0.1*	2.9 ± 0.1	7.1 ± 0.14	13.0 ± 0.13
Average TB spacing (nm)	45 ± 4.8	38.5 ± 5.2	34 ± 2.5	32.5 ± 3.2	30 ± 3.1
T_c (K)	89.9	90.2	90.3	90.4	90.4
$J_c^{\text{s.f.}}$ (77 K) (MA/cm²)	2.8	3.8	4.0	3.9	4.0

Table 1. Structural and superconducting properties. Sample data for the reference YBCO wire and for the (Y,Gd)BCO + BZO wires. $\delta\omega$ and $\delta\phi$ denote the full-width at half-maximum (FWHM) values of the out-of-plane rocking curves (ω scans) of the 005 diffraction peaks and in-plane rocking curves (ϕ scans) of the 103 diffraction peaks, respectively. The particle-size distribution was extracted from high-magnification planar- and cross-section views of several TEM images. The size of the BZO NPs ranged from 17 to 28 nm with a modal size of $\sim$23 nm. The average TB spacing was estimated from several planar view TEM images. T_c was determined using a criterion of $0.01\rho_n$. *225 precipitates.
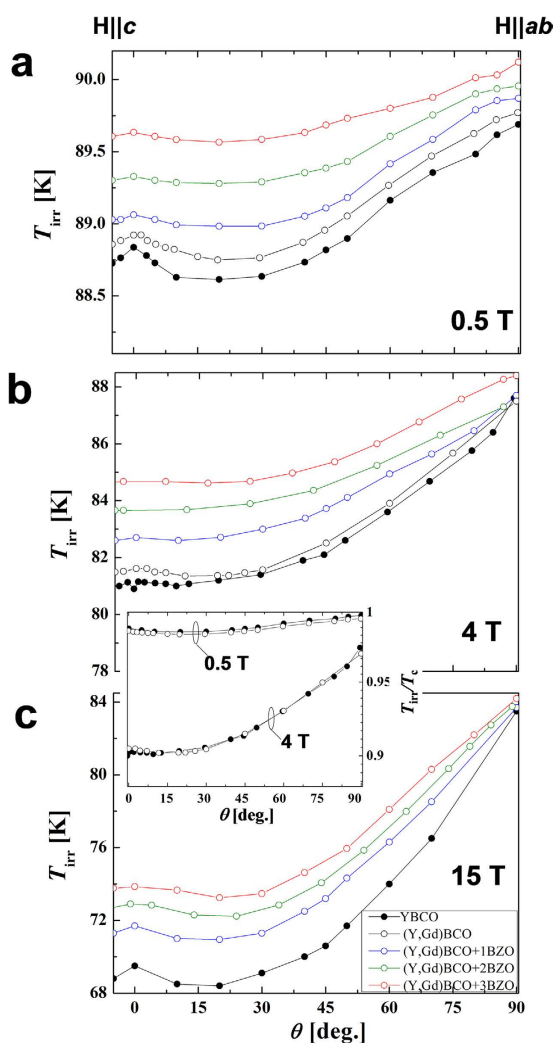

Figure 2. Angular dependent irreversibility temperature T_{irr}. Angular dependence of T_{irr} for YBCO, (Y,Gd) BCO and (Y,Gd)BCO+BZO wires at (**a**) 0.5 T, (**b**) 4 T and (**c**) 15 T, respectively. Inset of Fig. 2 indicates the angular dependent normalized T_{irr} (T_{irr}/T_c) for YBCO and (Y,Gd)BCO wires.
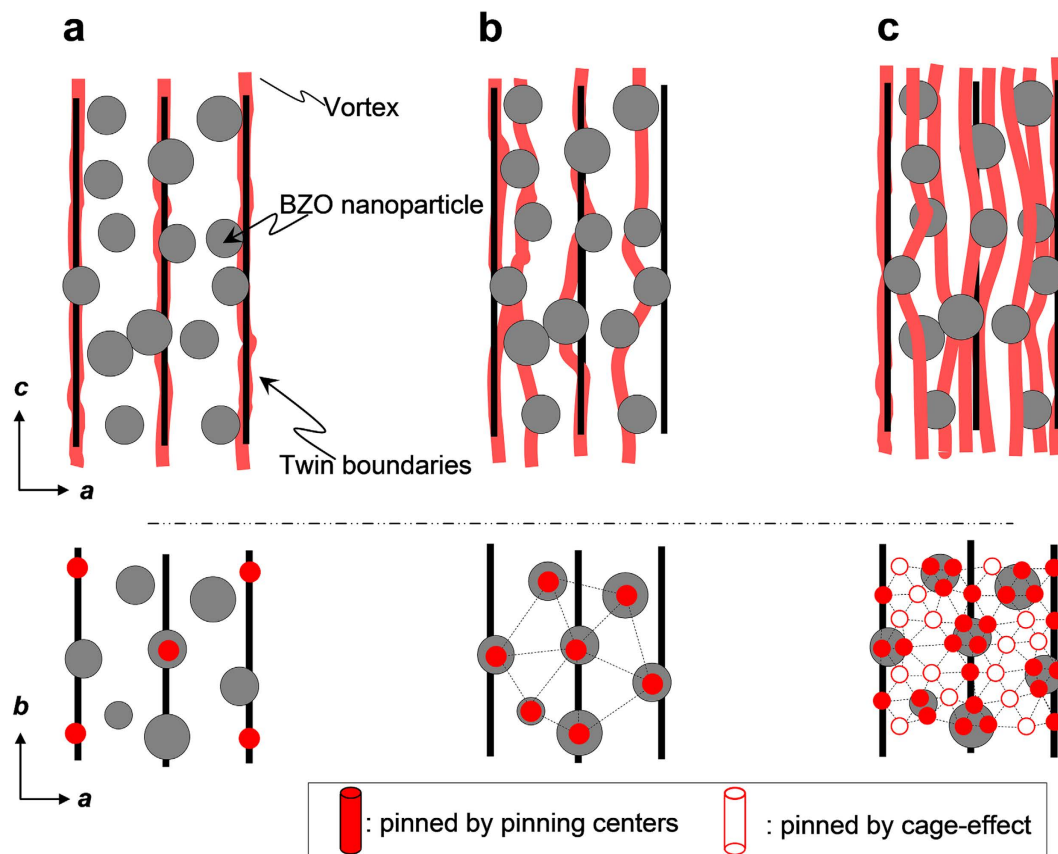
Figure 3. Diagrams of vortex pinning for configurations involving different defects at H∥c. (a) Diagram of vortex and c-axis parallel correlated TBs and BZO NPs at $\mu_0 H < \mu_0 H_{\phi,\text{TB}}$. **(b)** Diagram of a vortex and BZO NPs and TBs at $\mu_0 H \sim \mu_0 H_{\text{BZO}}(a_f = d_{\text{BZO}})$, showing that above $\mu_0 H_{\phi,\text{TB}}$ vortices are localized not only by TBs but also by BZO NPs. **(c)** Diagram of a vortex and hybrid defects at $\mu_0 H \gg \mu_0 H_{\text{BZO}}$, showing how a large number of vortices are arrested by BZO NPs and TBs.
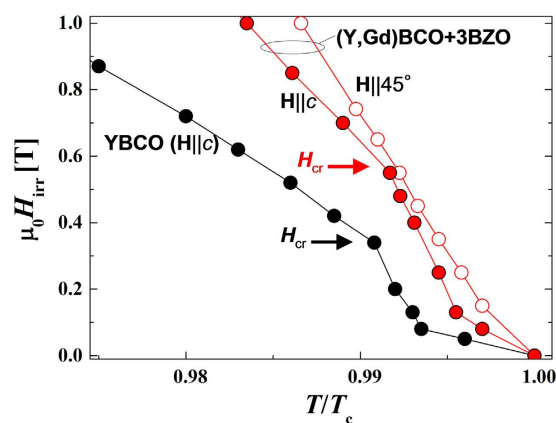

Figure 4. Temperature dependence of H_{irr} at low magnetic fields. Red open and solid symbol show $\mu_0 H_{\text{irr}}(T/T_c)$ at $\mathbf{H}\|45°$ and $\mathbf{H}\|c$, respectively, for the $+3$BZO wire. Black solid symbols indicate $\mu_0 H_{\text{irr}}(T/T_c)$ for the YBCO wire at $\mathbf{H}\|c$. A clear kink (H_{cr}) is observed only for $\mathbf{H}\|c$ for the wires.

decreasing T; above $\mu_0 H_{\text{cr}}$ the irreversibility line is closer to a linear temperature dependence. For the $+3$BZO wire, $\mu_0 H_{\text{cr}}$ is 0.55 T, which is 1.6 times higher than that of YBCO ($\mu_0 H_{\text{cr}} = 0.34$ T). From TEM images, we observe that this correlates with the higher TB density found in $+3$BZO as compared to YBCO wires. Indeed, we obtain $\mu_0 H_{\phi,\text{TB}} = 2.3$T and 1.0T, for $+3$BZO and YBCO, respectively. This cross-over is remarkably similar to that observed in YBCO bulk with nanoscale TBs[18,19] and columnar defects[20]. For TBs and columnar defects, the cross over field is usually not observed precisely at the matching field but around 1/3-1/2 of H_ϕ. This also correlates very well with our observation of the crossover fields with $H_{\text{cr}}/H_{\phi,\text{TB}} \sim 1/3$ for samples with and without BZO NPs,
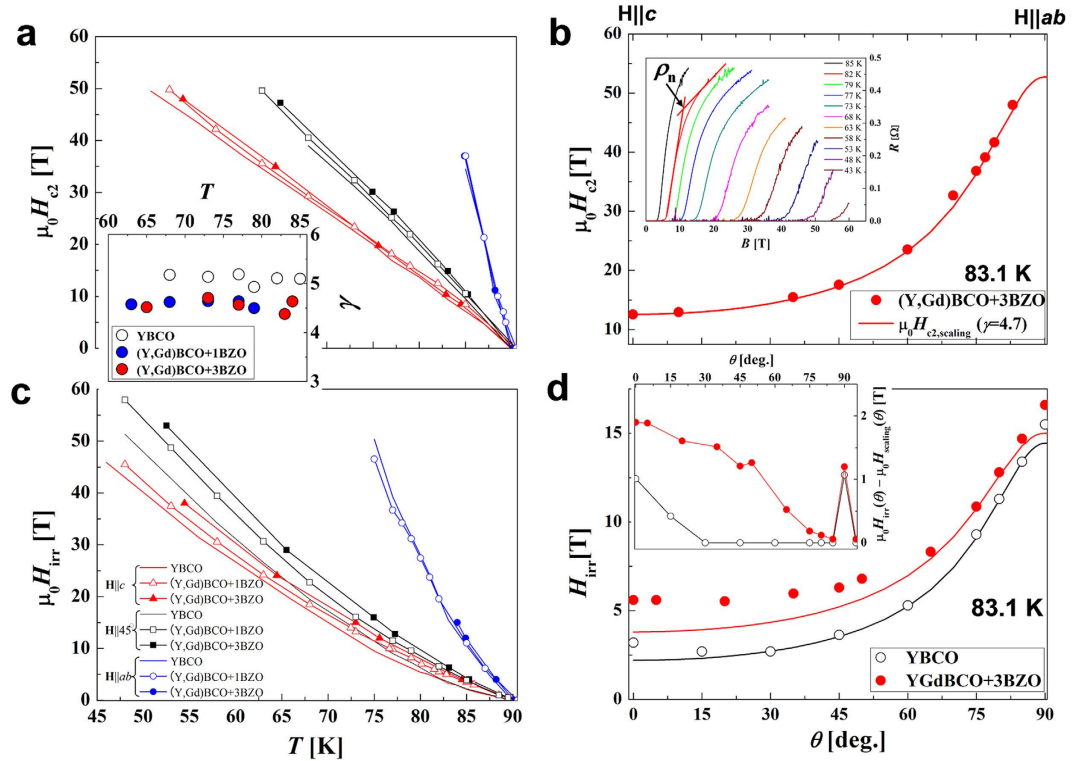
Figure 5. Temperature and angular dependence of the upper critical field and irreversibility field.
(**a**) Temperature and (**b**) angular dependence of $\mu_0 H_{c2}$. The inset of Fig. 5(a) shows the temperature dependence of γ calculated using $\mu_0 H_{c2}^{45}$ and $\mu_0 H_{c2}^{c}$. The inset of Fig. 5(b) shows $\rho_n(T)$ with $\mathbf{H}||c$ for YGdBCO + 1BZO wire. Solid lines in Fig. 5(b) are $\varepsilon(\theta)\mu_0 H_{c2}$ using γ values from the inset of Fig. 5(a). (**c**) Temperature and (d) angular dependence of $\mu_0 H_{irr}$. Solid lines in Fig. 5(d) are $\varepsilon(\theta)\mu_0 H_{irr}$ for the YBCO and +3BZO wires using $\gamma = 5.1$ and 4.7, respectively.

namely 0.34 and 0.24 for YBCO and +3BZO, respectively. To further corroborate that the observed crossover field arises from correlated defects and is not an artifact, we confirmed that no kink is found in H_{irr}-T at $\mathbf{H}||45°$ (see Fig. 4). Therefore, we can conclude that the array of TBs is the main source of correlated pinning at $\mathbf{H}||c$ in our MOD REBCO wires. Note that the TBs continue to contribute at $\mu_0 H \gg \mu_0 H_{cr}$ as seen in the peak of $T_{irr}(\theta)$ around $\mathbf{H}||c$ in Fig. 2c and the inset of Fig. 5d.

Irreversibility lines and upper critical fields in pulsed fields. To obtain the temperature and angular dependence of $\mu_0 H_{c2}$ and $\mu_0 H_{irr}$ for the YBCO and (Y,Gd)BCO + BZO wires at even higher fields, we measured $\rho(T)$ and $\rho(H)$ at various θ values by using pulsed fields up to 60 T (see insert Fig. 5b). See Methods for further details.

Figure 5a shows $\mu_0 H_{c2}(T)$ at $\mathbf{H}||c$, $\mathbf{H}||45°$, and $\mathbf{H}||ab$. The results demonstrate that $\mu_0 H_{c2}(T)$ is remarkably similar for all samples in spite of their very different pinning landscapes. The inset of Fig. 5a shows the electronic-mass anisotropy (γ) vs. T obtained from the H_{c2} measurements for the YBCO and (Y,Gd)BCO+BZO wires (see ref. 9 for details). The average values for γ are 5.1, 4.6 and 4.7 for the YBCO, +1BZO and +3BZO wires, respectively. Although γ is slightly smaller for the wires with BZO, all values are very close to 5. Further confirmation of the obtained value of γ, comes from the angular-dependent H_{c2} shown in Fig. 5b. The angular dependence of H_{c2} can be fit very well using $H\varepsilon(\theta) = H(\cos^2(\theta) + \gamma^{-2}\sin^2(\theta))$ (see ref. 21) with $\gamma = 4.7$, in agreement with the experimental result shown in the inset of Fig. 5a. This is also in accordance with our previous work, where we reported that the $\mu_0 H_{c2}(\theta)$ dependence follows a single curve consistent with $\gamma \sim 5$ even with different additions and growth methods[22]. From the $\mu_0 H_{c2}$ data, we conclude that $\mu_0 H_{c2}$ is not greatly affected by the pinning landscape. It is worth noting that the value of $\gamma \sim 5$ is indeed smaller than the values found for YBCO single crystals[23,24], as previously noted[25]. The lack of sensitivity in H_{c2} upon increase of disorder can be found in the small coherence length of REBCO (also the reason for high H_{c2}). The small coherence length places REBCO in the clean limit, thus making its superconducting properties less sensitive to disorder.

On the other hand, the changes in pinning landscape do influence H_{irr}, as a clear enhancement is found for all +BZO wires compared with YBCO wire (see Fig. 5c,d). Figure 5c displays the $\mu_0 H_{irr}$-T at various angles for the YBCO and (Y,Gd)BCO+BZO wires. For $\mathbf{H}||c$ and $\mathbf{H}||45°$, wires with BZO NPs show a higher $\mu_0 H_{irr}(T)$ than that of standard YBCO. Furthermore, we observe that $\mu_0 H_{irr}(T)$ continues to increases with higher densities of BZO NPs. For $\mathbf{H}||ab$, +BZO samples show a much smaller increase in $\mu_0 H_{irr}(T)$.

The changes can be better understood by analyzing the $H_{irr}(\theta)$ as shown in Fig. 5d. Consistent with Fig. 5c, the addition of BZO NPs produces a small increase near $\mathbf{H}||ab$ and a much bigger enhancement for $\mathbf{H}||c$ and
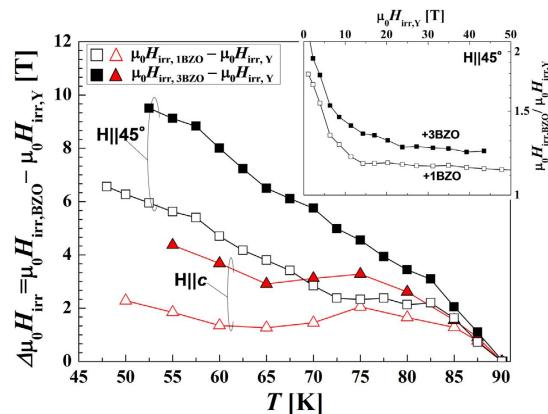
Figure 6. Temperature dependence of H_{irr} enhancement. Temperature dependence of $\Delta\mu_0 H_{irr} = \mu_0 H_{irr,BZO} - \mu_0 H_{irr,Y}$ at $\mathbf{H}||c$ and $\mathbf{H}||45°$ for $+1BZO$ and $+3BZO$ wires. The inset shows the ratio of $\mu_0 H_{irr,BZO}/\mu_0 H_{irr,Y}$ for $+1$ and $+3BZO$ for $\mathbf{H}||45°$.

intermediate orientations. The resulting angular dependence of H_{irr} for the $+3BZO$ wire cannot be described using the electronic-mass anisotropy scaling model, unlike $H_{c2}(\theta)$ or YBCO's $H_{irr}(\theta)$, which do follow $\varepsilon(\theta)$ for most of its angular dependence (see Fig. 5b,d). More information on the effect of the nanoparticles on H_{irr} can be observed in the inset to Fig. 5d. In this inset we plot the difference of $\mu_0 H_{irr}(\theta) - \varepsilon(\theta)\mu_0 H_{irr}$ for the YBCO and $+3BZO$ sample. For YBCO we observe that, except for the peaks around $\mathbf{H}||c$ and $\mathbf{H}||ab$ due to correlated disorder (TBs and SFs, respectively), over most of the angular range $H_{irr}(\theta)$ can be very well described by the electronic-mass anisotropy, $\gamma = 5$ indicating that most of the angular dependence of H_{irr} can be explained by pinning arising from weak random point defects such as oxygen vacancies (with diameter in the angstrom scale $\ll 2\xi(T)$). For $+3BZO$ we find very similar behavior near the ab-plane, where it shows a peak almost identical to that of the YBCO wire indicating similar ab-plane correlated pinning like SFs (consistent with $H_{irr}(T)$ in Fig. 5c). However, a much broader maximum is found for $|\theta| < 80°$. This is the consequence of the higher density of TBs coupled with the presence of strong random pinning from BZO NPs as shown in the TEM of Fig. 1b,c, and the schematics of Fig. 3. The NPs are responsible for the increases in the wider angular range and the TBs are more effective near the c axis. The broad dome-shape like increase in $\mu_0 H_{irr}(\theta) - \varepsilon(\theta)\mu_0 H_{irr}$ due to the NPs resembles the increases found in J_c in samples with nanosized inclusions, both in YBCO and Fe-based superconductors[10,26–29]. The reason for this dome shape (or inverse anisotropy) is found in the fact that while NPs are randomly dispersed, they are not point defects, thus do not follow the electronic mass anisotropy scaling as point defects do[21]. Recently Mishev *et al.* proposed a model to explain this effect based on the relative size of the vortex core compared to the inclusion size[29].

The leveling off observed in $H_{irr}(\theta)$ due to nanoparticles translates into an smaller ratio of $H_{irr}(||ab)/H_{irr}(||c)$, with values of 2.9 for $+3BZO$ as compared to 5.0 for YBCO. The decrease in the H_{irr} ratio (also found in J_c) has been analyzed using an 'effective anisotropy" (γ_{eff}) both for of $J_c(\theta)$ and $H_{irr}(\theta)$[6,7,30,31]. We attempted to scale the $H_{irr}(\theta)$ data of our BZO NPs doped wires using γ_{eff}. Using intermediate angles we obtain $\gamma_{eff} \sim 2$, but the scaling is not successful, as the data do not collapse onto a single curve as shown in the literature[6,7,30,31]. It is worth mentioning that although in principle the samples in references 6,7,14 are also MOD with NPs, there are some differences in the microstructure with the wires in this study. Specifically, with the addition of BZO our samples have a higher density of twin boundaries, but the opposite is found in ref. 14.

As shown in Fig. 5c, overall the $+3BZO$ wire shows an extremely high $\mu_0 H_{irr}$ at 65 K, at 30 T ($\mathbf{H}||45°$) and 24 T ($\mathbf{H}||c$) and at 50 K, 58 T ($\mathbf{H}||45°$) and 45 T ($\mathbf{H}||c$), values which to our knowledge are the highest reported for practical HTS wires[31] as well as for thin films on single-crystal substrates[32]. Recently, very high $\mu_0 H_{irr} = 14.8$ and 15.8 T at 77 K ($\mathbf{H}||c$) were observed in a heavily BZO nanorod-doped (Y,Gd)BCO wire grown by metal organic chemical vapor deposition[33,34] and BaHfO$_3$ doped PLD GdBCO wire[35]; these methods could also translate to great improvements of H_{irr} at high fields. This indicates that a high density of NPs/columns is beneficial not only for MOD prepared materials but is a general trend for REBCO wires.

Discussion

In order to pinpoint H-T regions where the BZO additions are more effective, in Fig. 6 we plot the H_{irr} enhancement $\Delta\mu_0 H_{irr} = \mu_0 H_{irr,BZO} - \mu_0 H_{irr,Y}$ for different concentrations of BZO NPs. This also set the bases to determine possible H-T saturation regions and if so, the dependence with magnetic field orientation. The improvement, $\Delta\mu_0 H_{irr}$, is bigger for higher BZO NP densities. We also find that ΔH_{irr} shows similar temperature dependences for samples with $+1BZO$, $+2BZO$ (not shown) and $+3BZO$ for all orientations measured. At $\mathbf{H}||45°$, $\Delta\mu_0 H_{irr}$ curves have a greater increase with respect to $\mathbf{H}||c$ for both concentrations, consistently with Fig. 5c, showing no signs of saturation up to the highest magnetic field measured.

The lack of saturation is also apparent in the inset of Fig. 6, which shows the ratio $\mu_0 H_{irr,BZO}/\mu_0 H_{irr,Y}$ for the $\mathbf{H}||45°$ orientation for two different concentrations of BZO NPs, 1% and 3%. The enhancement factor is largest at low fields and initially decays with H, but then becomes constant up the highest accessible fields. In particular, H_{irr} for $+3BZO$ is about 25% higher than for YBCO up to ~ 45 T.

Also observed in Fig. 6 is a steeper growth in H_{irr} at $T > 80\,K$ for both +1BZO and +3BZO wires. This temperature corresponds to $\mu_0 H \sim 5\,T$, where the inter-vortex distance is $a_f \sim 22\,nm$, which is close to the average BZO NP spacing ($d_{BZO} \sim 30\,nm$) observed in TEM images. This suggests that NPs are most effective in increasing $\mu_0 H_{irr}$ (at $\mathbf{H}\|45°$) when the intervortex spacing is similar the distance between NPs. This behavior is analogous to the J_c enhancement we observed as function of field for different NP densities in ref. 36.

The fact that improvements are smaller for $\mathbf{H}\|c$ compared to $\mathbf{H}\|45°$, is partly due to the fact that H_{irr} is already higher due to the presence of correlated defects (insert Fig. 5d). After an initial increase of H_{irr}, $\Delta\mu_0 H_{irr}$ flattens around 75 K and appears to increase again for $T < 60\,K$. The initial increase can be related to the higher density of NPs and/or of TBs, with the latter being 2.3 times more numerous in samples with BZO than in standard YBCO. However, the increase at lower temperatures is most likely related solely to the presence of nanoparticles, given the similarity of the behavior found at $\mathbf{H}\|45°$.

The lack of saturation in the increase of H_{irr} is remarkable. For +3BZO at $\mathbf{H}\|45°$ we have achieved a 25% enhancement up to the highest fields measured, with no sign of decrease. This corresponds to an absolute increase over 9 T for $\mu_0 H_{irr} \sim 50\,T$, implying an increase of ~ 4–$6\,K$ in operational temperature (depending on the orientation). This enhancement is particularly significant knowing that at $\mu_0 H \sim 60\,T$ the inter-vortex spacing is at least 7 times smaller than the average distance between nanoparticles. These findings indicate that further improvement of H_{irr} in practical REBCO wires is still possible, thus pushing the technically relevant region up to even higher magnetic fields.

In summary, we find that up to the highest BZO NPs density we tested, H_{irr} can be increased further, with no indication of saturation up to 60 T. This allows us to report extremely high $\mu_0 H_{irr}$, the highest values reported so far for REBCO films and wires. Our results suggest that higher densities of NPs will increase H_{irr} even more, and that the high-field limit is far from being reached in nanoengineered REBCO wires. These results are further proof that REBCO wire is an enabling technology for several high field applications.

Methods

HTS wires based on epitaxial REBCO nanocomposite films of standard YBCO and (Y,Gd)BCO + BZO were grown from metal organic solutions including Y-, Gd-, and Ba-trifluoroacetates and Cu-naphthenate with the cation ratio of 0.77 : 0.23 : 1.5 : 3 on ion-beam-assist deposited metal templates[37]. We added Zr-naphthenate into the (Y, Gd)BCO solutions; the content of BZO was 1–3wt%, and the concentration of starting solution was 1.2 mol/L. The total thickness of the superconductive layer for all samples was $0.5\,\mu m$, which was confirmed by cross sectional transmission electron microscopy (TEM). The details of the calcinations and conversion steps have been published elsewhere[17].

Films were patterned using photolithography and ion milling into bridges of $\sim 50\,\mu m$ width. The crystalline quality was examined by x-ray diffraction (XRD). The resistivity measurements, ρ vs. H, were realized in pulsed fields up to 60 T at the Pulsed Field Facility of the National High Magnetic Field Laboratory at Los Alamos National Laboratory. The four-probe technique was applied in AC mode with a low current corresponding to $400\,A/cm^2$ and a frequency of 100 kHz. Pulsed field measurements were performed at fixed orientations (θ), and the angular orientation was changed using a mechanical rotator. Additional ρ vs. T measurements were performed in a Quantum Design PPMS with a superconducting magnet (DC magnetic field) generating fields $\mu_0\mathbf{H}$ up to 15 T. For the transport measurements the current was always perpendicular to $\mathbf{H}$. Criteria of $0.9\rho_n$ and $0.01\rho_n$, where ρ_n is the normal state resistivity, were used to define H_{c2} and H_{irr}, respectively. Both planar and cross sectional TEM images were taken to evaluate the microstructure of the film.

The microstructures and elemental concentration mappings of the films were analyzed by transmission electron microscopy (TEM) and energy-dispersive x-ray spectroscopy (EDS), respectively.

References

1. Petrean, A. M., Paulius, L. M., Kwok, W. K., Fendrich, J. A. & Crabtree, G. W. Experimental evidence for the vortex glass phase in untwinned, proton irradiated $YBa_2Cu_3O_{7-\delta}$. *Phys. Rev. Lett.* **84,** 5852 (2000).
2. Krusin-Elbaum, L., Civale, L., Thompson, J. R. & Field, C. Accommodation of vortices to columnar defects: evidence for large entropic reduction of vortex localization. *Phys. Rev. B* **53,** 11744 (1996).
3. Olsson, R. J. *et al.* Bose glass transition in columnar-defected untwinned $YBa_2Cu_3O_{7-\delta}$. *Phys. Rev. B* **65,** 104520 (2002).
4. Horii, S. *et al.* Vortex Bose glass in $ErBa_2Cu_3O_y$ films with size-controlled nanorods. *Appl. Phys. Lett.* **93,** 152506 (2008).
5. Ozaki, T. *et al.* Flux pinning properties and microstructure of $SmBa_2Cu_3O_y$ thin films with systematically controlled $BaZrO_3$ nanorods. *J. Appl. Phys.* **108,** 093905 (2010).
6. Gutiérrez, J. *et al.* Strong isotropic flux pinning in solution-derived $YBa_2Cu_3O_{7-x}$ nanocomposite superconductor films. *Nat. Mat.* **6,** 367 (2007).
7. Puig, T. *et al.* Vortex pinning in chemical solution nanostructured YBCO films. *Supercond. Sci. Technol.* **21,** 34008 (2008).
8. Maiorov, B. *et al.* Synergetic combination of different types of defect to optimize pinning landscape using $BaZrO_3$-doped $YBa_2Cu_3O_7$. *Nat. Mat.* **8,** 398 (2009).
9. Miura, M. *et al.* Vortex liquid-glass transition up to 60 T in nanoengineered coated conductors grown by metal organic deposition. *Appl. Phys. Lett.* **96,** 072506 (2010).
10. Miura, M. *et al.* Mixed pinning landscape in nanoparticle-introduced $YGdBa_2Cu_3O_y$ films grown by metal organic deposition. *Phys. Rev. B* **83,** 184519 (2011).
11. Palau, A., Bartolomé, E., Llordés, A., Puig, T. & Obradors, X. Isotropic and anisotropic pinning in TFA-grown $YBa_2Cu_3O_{7-x}$ films with $BaZrO_3$ nanoparticles. *Supercond. Sci. Technol.* **24,** 125010 (2011).
12. Llordés, A. *et al.* Nanoscale strain-induced pair suppression as a vortex-pinning mechanism in high-temperature superconductors. *Nat. Mat.* **11,** 329 (2012).
13. Horide, T. *et al.* J_c improvement by double artificial pinning centers of $BaSnO_3$ nanorods and Y_2O_3 nanoparticles in $YBa_2Cu_3O_7$ coated conductors. *Supercond. Sci. Technol.* **26,** 075019 (2013).
14. Rouco, V. *et al.* Role of twin boundaries on vortex pinning of CSD YBCO nanocomposites. *Supercond. Sci. Technol.* **27,** 125009 (2014).

15. Sorbom, B. N. *et al.* ARC: A compact, high-field, fusion nuclear science facility and demonstration power plant with demountable magnets. *Fusion Engineering and Design* **100,** 378–405 (2015).
16. Wee, S. H., Zuev, Y. L., Cantoni, C. & Goyal, A. Engineering nanocolumnar defect configurations for optimized vortex pinning in high temperature superconducting nanocomposite wires. *Sci. Rep*. **3,** 2310 (2013).
17. Miura, M., Yoshizumi, M., Izumi, T. & Shiohara, Y., Formation mechanism of BaZrO$_3$ nanoparticles in Y$_{1-x}$Sm$_x$Ba$_2$Cu$_3$O$_y$-coated conductors derived from trifluoroacetate metal–organic deposition. *Supercond. Sci. Technol.* **23,** 014013 (2010).
18. Maiorov, B. & Osquiguil, E. Vortex solid state in YBa$_2$Cu$_3$O$_{7-\delta}$ twinned crystals. *Phys. Rev. B* **64,** 052511 (2001).
19. Shlyk, L. *et al.* Engineering periodic arrays of nanoscale twin boundaries in bulk YBa$_2$Cu$_3$O$_{7-\delta}$ with RuO$_2$ additions. *Appl. Phys. Lett.* **88,** 062509 (2006).
20. Civale, L. & Krusin-Elbaum, L. Comment on "Upper Limit of the Bose-Glass Transition in YBa$_2$Cu$_3$O$_7$ at High Density of Columnar Defects" *Phys. Rev. Lett.* **78,** 1829 (1997).
21. Blatter, G., Feigel'man, M. V., Geshkenbein, V. B., Larkin, A. I. & Vinokur, V. M. Vortices in high-temperature superconductors. *Rev. Mod. Phys.* **66,** 1125 (1994).
22. Holesinger, T., Maiorov, B. & Civale, L. Strategic materials development for enhanced coated conductor performance. Presented at 2010 Annual Peer Review for Advanced Cable and Conductors, Alexandria VA, USA, June 29-July 1, 2010, Available at:http://www.htspeerreview.com/pdfs/presentations/day%203/strategic-research/10_SR_StrategicMaterialsDevelopment_for_CoatedConductorPerformance.pdf (Accessed: 4 December 2015).
23. Maiorov, B., G. Nieva, G. & Osquiguil, E. First-order phase transition of the vortex lattice in twinned YBa$_2$Cu$_3$O$_7$ single crystals in tilted magnetic fields, *Phys. Rev. B* **61,** 12427–12432 (2000).
24. Kwok,W. K. *et al.* Vortex lattice melting in untwinned and twinned single crystals of YBa$_2$Cu$_3$O$_{7-\delta}$, *Phys. Rev. Lett.* **69,** 3370 (1992).
25. Civale, L. *et al.* Angular-dependent vortex pinning mechanisms in YBa$_2$Cu$_3$O$_7$ coated conductors and thin films , *Appl. Phys. Lett.* **84,** 2121 (2004).
26. Maiorov, B. *et al.* Vortex pinning landscape in YBa$_2$Cu$_3$O$_7$ films grown by hybrid liquid phase epitaxy. *Supercond. Sci. Technol.* **20,** S223 (2007).
27. Koshelev, A. E. & Kolton, A. B. Theory and simulations on strong pinning of vortex lines by nanoparticles. *Phys. Rev. B* **84,** 104528 (2011).
28. van der Beek, C. J., Konczykowski, M. & Prozorov, R. Anisotropy of strong pinning in multi-band superconductors. *Supercond. Sci. Technol.* **25** 084010 (2012).
29. Mishev, V. *et al.* Interaction of vortices in anisotropic superconductors with isotropic defects. *Supercond. Sci. Technol.* **28,** 102001(2015).
30. Chen, Z. *et al.* Three-dimensional vortex pinning by nano-precipitates in a Sm-doped YBa$_2$Cu$_3$O$_{7-x}$ coated conductor. *Supercond. Sci. Technol.* **20,** S205 (2007).
31. Tarantini, C. *et al.* Anisotropy of the irreversibility field for Zr-doped (Y,Gd)Ba$_2$Cu$_3$O$_{7-x}$ thin films up to 45 T. *Phys. Rev. B* **84,** 224514 (2011).
32. Rosenzweig, St. *et al.* Irreversibility field up to 42 T of GdBa$_2$Cu$_3$O$_{7-\delta}$ thin films grown by PLD and its dependence on deposition parameters. *Supercond. Sci. Technol.* **23,** 105017 (2010).
33. Selvamanickam, V. *et al.* High critical currents in heavily doped (Gd,Y)Ba$_2$Cu$_3$O$_x$ superconductor tapes. *Appl. Phys. Lett.* **106,** 032601 (2015).
34. Xu, A. *et al.* Strongly enhanced vortex pinning from 4 to 77 K in magnetic fields up to 31 T in 15 mol.% Zr-added (Gd,Y)-Ba-Cu-O superconducting tapes. *APL Mater.* **2,** 046111 (2014).
35. Awaji, S. *et al.* High-performance irreversibility field and flux pinning force density in BaHfO$_3$-doped GdBa$_2$Cu$_3$O$_y$ tape prepared by pulsed laser deposition. *Appl. Phys. Express* **8,** 023101 (2015).
36. Miura, M. *et al.* Strongly enhanced flux pinning in one-step deposition of BaFe$_2$(As$_{0.66}$P$_{0.33}$)$_2$ superconductor films with uniformly dispersed BaZrO$_3$ nanoparticles. *Nat. Commun.* **4,** 2499 (2013).
37. Yamada, Y. *et al.* Development of Long Length IBAD-MgO and PLD Coated Conductors. *IEEE Trans. Appl. Supercond.* **19** 3236 (2009).

Acknowledgements

Author Contributions

M.M. grew the films, carried out the experimental design, performed the superconducting property measurements and prepared the manuscript. B.M. carried out superconducting property measurements, data analysis, provided advice and consultation on flux pinning and assisted in preparing the manuscript and coordinated the research. F.F.B. carried out superconducting properties measurement. T.K. carried out microstructural studies. M.S. carried out superconducting property measurements. Y.T. carried out photolithography preparations. T.I. provided advice and consultation on film preparation. L.C. contributed to discussion and manuscript preparation. All authors discussed the results and implications and commented on the manuscript.

Additional Information

Competing financial interests: The authors declare no competing financial interests.

How to cite this article: Miura, M. *et al.* Upward shift of the vortex solid phase in high-temperature-superconducting wires through high density nanoparticle addition. *Sci. Rep.* **6**, 20436; doi: 10.1038/srep20436 (2016).